

Article

# A Facile One-Pot Synthesis of Water-Soluble, Patchy Fe<sub>3</sub>O<sub>4</sub>-Au Nanoparticles for Application in Radiation Therapy

Stefanie Klein <sup>1</sup>, Jakob Hübner <sup>2</sup>, Christina Menter <sup>1</sup>, Luitpold V. R. Distel <sup>3</sup>,  
Winfried Neuhuber <sup>4</sup>  and Carola Kryschi <sup>1,\*</sup> 

<sup>1</sup> Department Chemistry and Pharmacy, Physical Chemistry I and ICMM, Friedrich-Alexander University of Erlangen, Egerlandstr. 3, D-91058 Erlangen, Germany; stefanie.klein@fau.de (S.K.); christina.menter@fau.de (C.M.)

<sup>2</sup> French-German Research Institute of Saint-Louis, 5 rue du Général Cassagnou, F-68300 Saint-Louis, France; jakob.huebner@isl.eu

<sup>3</sup> Department of Radiation Oncology, Friedrich-Alexander University of Erlangen, Universitätsstr. 27, D-91054 Erlangen, Germany; luitpold.distel@uk-erlangen.de

<sup>4</sup> Department of Anatomy, Chair of Anatomy I, Friedrich-Alexander University of Erlangen, Krankenhausstr. 9, D-91054 Erlangen, Germany; winfried.neuhuber@fau.de

\* Correspondence: carola.kryschi@fau.de; Tel.: +49-9131-85-27307

Received: 15 November 2018; Accepted: 18 December 2018; Published: 21 December 2018



**Abstract:** A facile one-pot synthesis route for the preparation of water-soluble, biocompatible patchy Fe<sub>3</sub>O<sub>4</sub>-Au nanoparticles (Fe<sub>3</sub>O<sub>4</sub>-Au pNPs) was developed. Biocompatibility was attained through surface functionalization with 1-methyl-3-(dodecylphosphonic acid) imidazolium bromide. The morphology, composition, crystal structure and magnetic properties of the Fe<sub>3</sub>O<sub>4</sub>-Au pNPs were investigated by conducting experiments with transmission electron microscopy, energy dispersive X-ray spectroscopy, X-ray diffraction and superconducting quantum interference device, respectively. Internalization of the Fe<sub>3</sub>O<sub>4</sub>-Au pNPs by MCF-7 cells occurred via endocytosis. The performance of the Fe<sub>3</sub>O<sub>4</sub>-Au pNPs as X-ray radiosensitizer in tumor cells was compared with that of gold nanocluster and Fe<sub>3</sub>O<sub>4</sub> NPs. For this reason, MCF-7, A549 and MCF-10A cells were loaded with the respective kind of nanoparticles and treated with X-rays at doses of 1, 2 or 3 Gy. The nanoparticle-induced changes of the concentration of the reactive oxygen species (ROS) were detected using specific assays, and the cell survival under X-ray exposure was assessed employing the clonogenic assay. In comparison with the gold nanocluster and Fe<sub>3</sub>O<sub>4</sub> NPs, the Fe<sub>3</sub>O<sub>4</sub>-Au pNPs exhibited the highest catalytic capacity for ROS generation in MCF-7 and A549 cells, whereas in the X-ray-induced ROS formation in healthy MCF-10A cells was hardly enhanced by the Fe<sub>3</sub>O<sub>4</sub> NPs and Fe<sub>3</sub>O<sub>4</sub>-Au pNPs. Moreover, the excellent performance of Fe<sub>3</sub>O<sub>4</sub>-Au pNPs as X-ray radiosensitizers was verified by the quickly decaying radiation dose survival curve of the nanoparticle-loaded MCF-7 and A549 cells and corroborated by the small values of the associated dose-modifying factors.

**Keywords:** X-ray radiosensitizer; radiotherapy; patchy Fe<sub>3</sub>O<sub>4</sub>-Au nanoparticles; MCF-7 cells; A549 cells; MCF-10A cells

## 1. Introduction

Over the last century, high-energy radiation, and in particular X-rays, has been utilized to treat cancer. The underlying concept is that rapidly proliferating cancer cells are more sensitive to X-rays than healthy cells [1]. X-ray irradiation of the cytoplasm causes radiolysis of water and gives rise to the formation of reactive oxygen species (ROS), including the super oxide radical (O<sub>2</sub><sup>•-</sup>), hydrogen

peroxide ( $\text{H}_2\text{O}_2$ ) and hydroxyl radical ( $\text{HO}^\bullet$ ). The most reactive one,  $\text{HO}^\bullet$ , provokes severe cellular damage, as it interacts with all biological molecules. This may give rise to lipid peroxidation, protein damage, deoxyribonucleic-acid strand breakages and membrane destruction which results in apoptotic and necrotic cell death.

Despite substantial advances in the progress of novel cancer therapies such as the successful development of brachytherapy and intensity-modulated radiotherapy, nowadays, the greatest challenge is still to expose tumor cells to a lethal dose of X-rays while sparing normal cells [2]. An encouraging approach is the application of nanoparticulate radiosensitizers to tumor tissue which boosts the impact of X-rays on tumor cells [3–9]. Local dose enhancement in radiotherapy of cancer employs high-Z materials (e.g., gold, platinum, bismuth and gadolinium), as they exhibit a large photoelectric absorption coefficient [5]. Interaction between X-rays with moderate energies (10 to 500 keV) and high-Z gold atoms in nanoparticles generates secondary electrons, such as photoelectrons and Auger electrons [4,8]. Since the range of these electrons is very short, they are highly effective in close proximity to gold nanoparticles inside the tumor cell. X-radiation-induced emission of these short-range electrons facilitates the deposition of highly localized energy into the cellular organelles, which inflicts irreversible damage to the targeted cells. On the other hand, due to their rapid decay within nanoscale volumes, these electrons cannot impair the surrounding healthy tissue. Therefore, gold nanoparticles (AuNPs) are auspicious candidates for application as radio-enhancers for X-rays in radiotherapy [6,10–12].

The most effective reactive oxygen species (ROS), which are generated by X-ray irradiation of intracellular AuNPs, are the superoxide anion ( $\text{O}_2^{\bullet-}$ ) and hydroxyl radical ( $\text{HO}^\bullet$ ). X-ray-triggered generation of photoelectrons and Auger electrons is understood to be responsible for the formation of  $\text{O}_2^{\bullet-}$  in the vicinity of gold nanoparticles, whereas the emitted characteristic X-radiation causes the formation of  $\text{HO}^\bullet$  due to water radiolysis [13]. Among these ROS, the  $\text{HO}^\bullet$  causes the greatest damage to tumor cells by oxidizing lipids, proteins and DNA [14]. In recent studies [15,16], we could unambiguously prove that intracellular  $\text{Fe}_3\text{O}_4$  nanoparticles (SPIONs) enhanced the impact of X-radiation on tumor cells by significantly increasing the ROS production and, in particular, by raising the intracellular  $\text{HO}^\bullet$  concentration. The radio-enhancing effect of the SPIONs originates from the catalytic activity of their surfaces. X-rays, even at 1 Gy, verifiably destroy the coating of intracellular SPIONs terminated with citrate or malate moieties. X-radiation-induced ablation of the surface layer of the SPIONs creates highly reactive surfaces containing  $\text{Fe}^{3+}$  and  $\text{Fe}^{2+}$  ions that catalyze the ROS formation via the Fenton mechanism and Haber-Weiss cycle. The ROS concentration was found to be increased by more than 300% [16].

Another encouraging approach for radio-enhancing nanomaterials is based on the fusion of plasmonic gold and superparamagnetic  $\text{Fe}_3\text{O}_4$  nanoparticles yielding  $\text{Fe}_3\text{O}_4$ -Au nanocomposites. In the recent past, sophisticated synthesis strategies for the preparation of  $\text{Fe}_3\text{O}_4$ -Au nanocomposites have facilitated the realization of diverse magnetoplasmonic nanoparticles, including core-shell, flower-like and dumbbell-like nanoheterostructures [17]. For instance,  $\text{Fe}_3\text{O}_4$ @Au core-shell nanoparticles exhibit an encouraging potential for biomedical applications [18–22], since the gold surface provides biocompatibility and, furthermore, may be easily functionalized in aqueous solutions with thiol-containing biomolecules. Unfortunately, the complete gold shell also limits the radio-enhancing performance, because it completely blocks the catalytic activity of the  $\text{Fe}_3\text{O}_4$  nanoparticle surface. In contrast, dumbbell-like Au- $\text{Fe}_3\text{O}_4$  nanoheterodimers should be perfectly tailored for their application as radio-enhancing agents, since such nanoheterodimers unify the high-Z material and the  $\text{Fe}_3\text{O}_4$  catalyst surface [23,24]. However, the major drawback of the Au- $\text{Fe}_3\text{O}_4$  nanodumbbells concerns their surfaces, which are irreversibly stabilized with oleic acid, completely hampering their solubility in aqueous solution. The surfactants oleic acid and oleylamine are essential for the synthesis of Au- $\text{Fe}_3\text{O}_4$  nanodumbbells, which only succeeds through thermal decomposition of an iron precursor (e.g.,  $\text{Fe}(\text{CO})_5$ ,  $\text{Fe}(\text{acac})_3$ ) on AuNPs in the presence oleic acid and oleylamine at temperatures above 300 °C [16,25–27].

In this contribution, we report a novel, simple, one-pot synthesis route enabling the preparation of water-soluble, non-toxic patchy  $\text{Fe}_3\text{O}_4$ -Au nanoparticles, which exhibit an encouraging radiosensitizer potential for cancer therapy. The patchy surface architecture emerges from growing gold nanoclusters on the  $\text{Fe}_3\text{O}_4$  nanoparticle surface. Surface-grown Au nanopatches are expected to enhance the radio-catalytic activity of the  $\text{Fe}_3\text{O}_4$  nanoparticles due to interfacial communication [26]. X-ray irradiation of intracellular  $\text{Fe}_3\text{O}_4$ -Au nanoparticles may result in  $\text{Fe}_3\text{O}_4$  surface-catalyzed production of ROS and the generation of  $\text{O}_2^{\bullet}$  near the Au surface, which is significantly enhanced by interfacial electron transfer and excess electronic charges (hot spots) at the Au surface [27]. To attain biocompatibility and water solubility, the as-synthesized patchy  $\text{Fe}_3\text{O}_4$ -Au nanoparticles ( $\text{Fe}_3\text{O}_4$ @Au pNPs) were successfully stabilized with 1-methyl-3-(dodecylphosphonic acid) imidazolium, forming a self-assembled monolayer on the nanoparticle surface. Different kinds of tumor cells (MCF-7 and A549) loaded with  $\text{Fe}_3\text{O}_4$ @Au pNPs and exposed to X-radiation in a single dose of 1 Gy were shown to increase the relative ROS concentration by more than 130%. The associated dose-modifying factors (DMF) reached values of 0.448 and 0.422, demonstrating the excellent performance of the  $\text{Fe}_3\text{O}_4$ @Au pNPs as X-ray dose-enhancing agents.

## 2. Materials and Methods

**Chemicals.**  $\text{HAuCl}_4 \times 3\text{H}_2\text{O}$  ( $\geq 99.5\%$ ) was purchased from Carl Roth.  $(\text{NH}_4)_2\text{Fe}(\text{SO}_4)_2 \times 6\text{H}_2\text{O}$  ( $\geq 99\%$ ),  $\text{FeCl}_3 \times 6\text{H}_2\text{O}$  (97%), 3-mercaptopropionic acid ( $\geq 99\%$ ),  $\text{NaBH}_4$  ( $\geq 96\%$ ), ethanol ( $\geq 95\%$ ), fetal calf serum (FCS), penicillin-streptomycin-solution, sodium pyruvate, phosphate buffered saline (PBS), non-essential amino acids (MEM), trypsin/EDTA, 3-amino-7-dimethylamino-2-methyl-phenazine hydrochloride (neutral red), crystal violet (98%), and 2',7'-dichlorofluorescein diacetate (DCFH-DA) (95%) were bought from Sigma-Aldrich (Munich, Germany, 2018). 1-methyl-3-(dodecylphosphonic acid) imidazolium bromide from Sikémia (Montpellier, France, 2018). DMEM, GlutaMAX Supplement, MitoSOX<sup>TM</sup> Red Mitochondrial Superoxide Indicator and 3-(p-hydroxyphenyl) fluorescein (HPF) from Thermo Fischer Scientific (Karlsruhe, Germany, 2018) and glacial acetic acid and DMSO (99.7%) from Merck. Millipore (Darmstadt, Germany, 2018) water was used in all experiments.

**Synthesis of the  $\text{Fe}_3\text{O}_4$ @Au pNPs.** 3-Mercaptopropionic acid (MPA) stabilized  $\text{Fe}_3\text{O}_4$ @Au pNPs were obtained through alkaline co-precipitation of  $\text{Fe}_3\text{O}_4$  NPs in aqueous  $\text{HAuCl}_4$  solution, and were subsequently stabilized with 3-mercaptopropionic acid (MPA). 21 mL HCl solution was prepared by adding 1 mL of 1 M HCl to 20 mL of water. This solution was heated up to 80 °C under stirring. 2 mL of aqueous  $\text{HAuCl}_4$  solution (25 mM) were added at once. 3 mL of aqueous ammonium iron(II) sulfate hexahydrate solution (100 mM) and 0.05 mL of aqueous MPA (10 mM) solution were added. After a reaction time of 1 min 3 mL ammonia (30 wt.%) were added. The resulting black suspension was refluxed for 30 min. The resulting MPA-stabilized  $\text{Fe}_3\text{O}_4$ @Au pNPs were collected by magnetic decantation and washed thrice with 20 mL ultrapure water.

**Synthesis of  $\text{Fe}_3\text{O}_4$  nanoparticles.**  $\text{Fe}_3\text{O}_4$  nanoparticles ( $\text{Fe}_3\text{O}_4$  NPs) were synthesized following Massart's procedure under argon [28].

**Surface-coating procedure.** For attaining biocompatibility, the initially MPA-stabilized  $\text{Fe}_3\text{O}_4$ @Au pNPs and pristine  $\text{Fe}_3\text{O}_4$  NPs were coated with 1-methyl-3-(dodecylphosphonic acid) imidazolium bromide (Imidazolium-PA). 15 mg of the  $\text{Fe}_3\text{O}_4$ @Au pNPs or  $\text{Fe}_3\text{O}_4$  NPs were dispersed in water by sonication. Afterwards 40 mM of a methanolic solution of Imidazolium-PA were subjoined, and the mixture was sonicated for 30 min. The  $\text{Fe}_3\text{O}_4$ @Au pNPs and  $\text{Fe}_3\text{O}_4$  NPs were magnetically isolated and washed thrice. For the  $\text{Fe}_3\text{O}_4$  NPs the whole procedure was carried out under argon.

**Synthesis of gold nanocluster.** MPA-stabilized gold nanoclusters (AuNCs) were prepared by dissolving  $\text{HAuCl}_4$  (35.7  $\mu\text{mol}$ ) in methanol (7 mL), followed by the addition of MPA (142.8  $\mu\text{mol}$ ). The mixture was cooled in an ice bath for 30 min.  $\text{NaBH}_4$  dissolved in water (0.2 M, 357  $\mu\text{mol}$ , 0 °C), was then rapidly injected into the  $\text{AuCl}_4^-$ -MPA-mixture under vigorous stirring. The reaction mixture changed its color to dark red-brown under bubbling with nitrogen. After 1 hour of reaction in the ice bath, the mixture was centrifuged (8500 rpm, 10 min). The collected precipitate was subsequently

washed with methanol and after the removal of the solvent the precipitate was dried in vacuum and the product was obtained as a black powder.

*Characterization of the nanoparticles.* UV-Vis absorption and Fourier-Transform Infrared (FTIR) spectra were measured using a Perkin Elmer Lambda 2 (Perkin Elmer, Rodgau, Germany, 1987) and a Shimadzu IR Prestige-21 (Shimadzu Europa GmbH, Duisburg, Germany, 2002) device, respectively. The FTIR spectra were obtained in the attenuated total reflectance (ATR) mode on a diamond/ZnSe crystal plate (MIRacle ATR, Pike Technologies, Madison, WI, USA, 2015). Experiments with energy dispersive X-ray spectroscopy (EDX) were performed using a QUANTAX EDS system (Bruker Nano GmbH, Berlin, Germany, 2012). Transmission electron microscopy (TEM) images were taken with a Zeiss EM 900 TE microscope (Carl Zeiss GmbH, Oberkochen, Germany, 2010). This TE microscope has a nominal point resolution of 5.0 Å at Scherzer defocus and was operated at an acceleration voltage of 80 kV. High resolution transmission electron microscopy (HRTEM) was applied using a Phillips CM 300 UltraTWIN TE microscope (Philips, Eindhoven, The Netherlands, 2000) at an acceleration voltage of 300 kV with a nominal point resolution of 1.7 Å at Scherzer defocus. The EDX spectra were acquired using a Super-X detector. The samples for the TEM und HRTEM investigations were obtained by drop-casting the Fe<sub>3</sub>O<sub>4</sub>@Au pNPs solution on amorphous holey carbon film coated copper TEM grids. The XRD scans were measured in the Bragg-Brentano geometry by means of a Bruker AXS Advance D8 (Bruker Nano GmbH, Berlin, Germany, 2015) X-ray diffractometer using Cu K<sub>α</sub> radiation ( $\lambda_{K\alpha} = 1.54 \text{ \AA}$ ) at an acceleration voltage of 30 kV. The magnetization curves and ZFC/FC *vs.* temperature plots of the Fe<sub>3</sub>O<sub>4</sub>@Au pNPs and Fe<sub>3</sub>O<sub>4</sub> NPs were recorded on a Quantum Design MPMS-XL5 SQUID magnetometer (Quantum Design Inc., San Diego, CA, USA, 2015).

*Cell experiments.* The biocompatibility and the diverse ROS assays were executed by means of a Synergy HT microplate reader (BioTek Inc., Winooski, VT, USA, 2016). TEM images of MCF-7 cells incorporating Fe<sub>3</sub>O<sub>4</sub>@Au pNPs were obtained with a Zeiss EM 906 (Carl Zeiss GmbH, Oberkochen, Germany, 1993). The diverse kinds of cell lines (i.e., MCF-7, MCF-10A and A459) were exposed to X-radiation generated by a 120 kV X-ray tube equipped with a tungsten anode (Comet MXR 160/0.4-3.0, Comet, Flamatt, Switzerland, 2011). The X-radiation has an on average energy value of 34 keV and a maximum energy value of 120 keV.

*Cell culture.* The MCF-7, MCF-10A and A459 cells were cultured in DMEM containing 4500 mg glucose/L, enriched with 10% fetal calf serum (FCS), 1 mM sodium pyruvate, 100 U/mL penicillin, 100 µg/mL streptomycin, 2 mM L-glutamine and 1% MEM nonessential amino acids. The cells were incubated in a humidified environment of 5% CO<sub>2</sub> at 37 °C and sub-cultivated twice a week.

*Neutral red assay.* The MCF-7, MCF-10A and A459 cells were seeded in 96-well plates at a cell per well density of  $2-3 \times 10^4$  and were incubated overnight. The cell culture medium was replaced by a medium containing the Fe<sub>3</sub>O<sub>4</sub>@Au pNPs, Fe<sub>3</sub>O<sub>4</sub> NPs or gold nanocluster (AuNC) at a concentration of 10 µg/mL. Subsequently to 24 h incubation, the cell medium was substituted by an FCS-free medium containing 40 µg/mL neutral red (NR). After 2 h incubation at 37 °C, the NR-enriched medium was aspirated off, and the cells were rinsed with PBS. NR molecules trapped inside the lysosomes were released by the addition of 100 µL/well dye-destaining solution (50% ethanol, 49% water, 1% glacial acetic acid). The absorbance of the NR solution was measured at 540 nm.

*Cell preparation for TEM examinations.* MCF-7 cells were incubated overnight with culture medium containing the Fe<sub>3</sub>O<sub>4</sub>@Au pNPs at a concentration of 10 µg/mL. The cells were washed with ice-cold PBS (pH 7.4), were subsequently fixed with 2.5% glutaraldehyde at 4 °C (overnight) and then post-fixed in 1% OsO<sub>4</sub> and 3% K<sub>3</sub>Fe(CN)<sub>6</sub> at room temperature. Thereafter, the cells were dehydrated in ethanol and encapsulated in Epon. 60–70-nm-thick slices were obtained with an ultramicrotome and mounted on Epon blocks. Non-contrasted silver-grey ultrathin slices were imaged.

*ROS, superoxide and hydroxyl radical assays.* The MCF-7, MCF-10A and A459 cells were seeded in 96-well plates at a cell per well density of  $2-3 \times 10^4$  and were incubated overnight. The cell medium was substituted by one containing the NPs at a concentration of 10 µg/mL. After 24 h incubation, the NP-enriched medium was aspirated off. According to the different assay protocols the respective

dye solution was filled in. Subsequently, half of the 96-well plates were treated with X-rays at a single dose of 1 Gy.

**ROS assay.** 2',7'-dichlorofluorescein diacetate (DCFH-DA) was dissolved in DMSO to obtain a 0.01 M stock solution which was diluted with DMEM to 100  $\mu$ M. The cells were incubated in this solution for 30 min. After cellular uptake, the acetate groups of DCFH-DA were cleaved off so that the DCFH molecules remained inside the cells. Afterwards, the wells were washed with PBS and 100  $\mu$ L PBS were added in each well. The cells were exposed to X-radiation or remained non-irradiated. ROS oxidize intracellular DCFH to fluorescent DCF. Upon excitation at 480 nm the fluorescence emission of the DCF dye was detected at 528 nm.

**Superoxide assay.** The relative intracellular concentration of superoxide radicals ( $O_2^{\bullet-}$ ) was determined by means of the MitoSOX<sup>TM</sup> Red mitochondrial superoxide indicator, following the manufacturer's protocol. The dye was dissolved in DMSO at a concentration of 2.5 mM and diluted to 5  $\mu$ M in Hank's balanced salt solution (HBSS). After 10 min incubation followed by X-ray irradiation, the cells were washed and 100  $\mu$ L of HBSS were added. The fluorescence of MitoSOX<sup>TM</sup> Red was excited at 530 nm, and the fluorescence intensity was detected at 590 nm.

**Hydroxyl radical assay.** 3'-(p-hydroxyphenyl)-fluorescein (HPF) selectively reacts with  $HO^{\bullet}$ . The 5 mM HPF solution was diluted to 5  $\mu$ M in Krebs-Ringer buffer. After removal of the cell culture medium, 100  $\mu$ L of HPF solution is added, and the cells were incubated therein for 30 min. Then the cells were washed and exposed to X-radiation. The fluorescence emission of intracellular HPF was excited at 490 nm and detected at 515 nm.

**Clonogenic cell survival assay.** The MCF-7, MCF-10A and A459 cells were grown in 6-well plates and were incubated in culture medium enriched with the respective kind of NPs (10  $\mu$ g/mL) overnight. After X-ray irradiation at single dosages of 1, 2 or 3 Gy, the cells were detached, seeded and grown in 6-well plates for 2 weeks to form colonies. The cell colonies were fixed and stained with a mixture of 0.5% (*w/v*) crystal violet in 50/50 methanol/water for 30 min. Colonies containing more than 50 cells were counted. The colony number was used to calculate the surviving fraction (SF). The survival curves were fitted to a linear quadratic function ( $\ln SF = -(\alpha D + \beta D^2)$ ). The X-ray enhancing effect was assessed by determining the dose modifying factor (DMF) from the X-radiation survival curves upon calculating the ratio of radiation doses at the 50% survival level (NP-treated radiation dose divided by the control radiation dose).

**Statistical Analysis.** Data are presented as arithmetic mean values  $\pm$  standard error (SE). Statistical analysis was performed using the analysis of variance (ANOVA) with post hoc Bonferroni correction for multiple comparisons. A value of  $p < 0.05$  was considered to be statistically significant.

### 3. Results

Patchy  $Fe_3O_4$ -Au nanoparticles ( $Fe_3O_4@Au$  pNPs) were obtained through alkaline co-precipitation of  $Fe_3O_4$  nanoparticles from an aqueous ferrous and ferric solution in presence of Au nanostructures which were formed before through reduction of  $Au^{3+}$  cations by  $Fe^{2+}$  cations in acidic solution. The  $Fe_3O_4@Au$  pNPs were stabilized by subsequent treatment with 3-mercaptopropionic acid (MPA) and 1-methyl-3-(dodecylphosphonic acid) imidazolium bromide (Imidazolium-PA). The formation of the  $Fe_3O_4@Au$  pNPs was confirmed by examining their composition, structure, morphology and magnetic properties using EDX, XRD, HRTEM, and SQUID. The EDX spectrum of the  $Fe_3O_4@Au$  pNPs indicates the content of Fe, O and Au in the nanoparticles (Figure 1a). The atomic ratio of Fe to Au is 9:1, which suggests that the  $Fe_3O_4$  NPs were the main component and formed the core. The powder XRD pattern in Figure 1b displays the characteristic peaks of  $Fe_3O_4$  in the cubic inverse spinel structure and those of the Au nanostructures in the fcc phase. The peaks at  $2\Theta = 30.52^\circ, 35.91^\circ, 43.59^\circ, 53.91^\circ, 57.43^\circ,$  and  $63.13^\circ$  are attributed to diffraction from the (220), (311), (400), (422), (511), and (440) planes of  $Fe_3O_4$ , whereas the diffraction peaks at  $38.50^\circ, 44.47^\circ, 64.75^\circ, 77.54^\circ$  and  $81.74^\circ$  are assigned to the (111), (200), (220), (311), and (222) planes of gold. The relatively broad widths (FWHM  $> 0.8^\circ$ ) of the diffraction peaks correlate with the ultra-small sizes of the  $Fe_3O_4$  and Au nanostructures. The mean crystal size of

the  $\text{Fe}_3\text{O}_4$  nanoparticles was determined from the XRD pattern using Debye-Scherrer's equation and the highest-intensity diffraction peak of the (311) facet [29]. The calculated nanoparticle diameter is 22 nm. More detailed information on the morphology and size distribution of the  $\text{Fe}_3\text{O}_4@Au$  pNPs were attained by conducting a TEM analysis. The NP size distribution was determined by measuring the diameters of 110 NPs. Figure 2 depicts a representative TEM image (a) and the nanoparticle-size histogram (b), the latter was fitted to a Gaussian function (red solid line). The  $\text{Fe}_3\text{O}_4@Au$  pNPs exhibit nearly spherical shapes and sizes between 8 and 22 nm with a mean value of 12.5 nm.

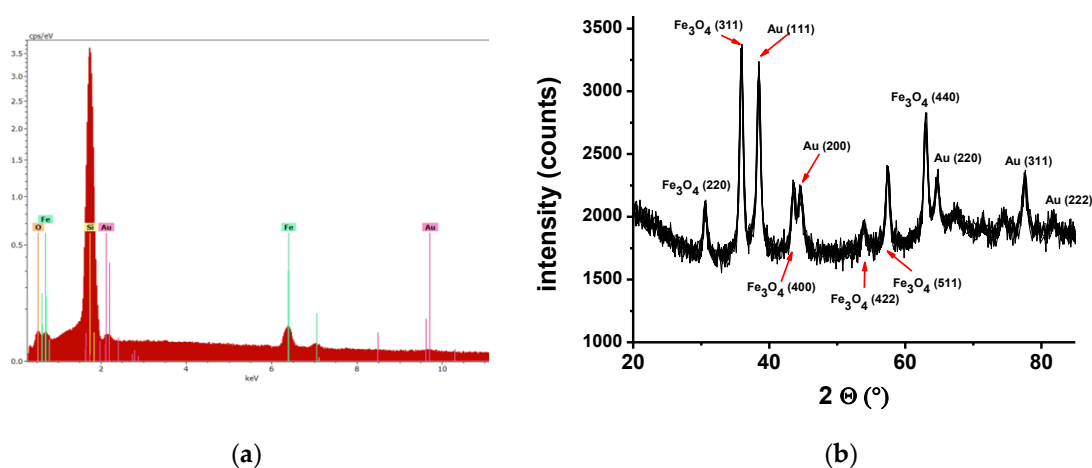


Figure 1. (a) EDX analysis of  $\text{Fe}_3\text{O}_4@Au$  pNPs; (b) XRD pattern of  $\text{Fe}_3\text{O}_4@Au$  pNPs.

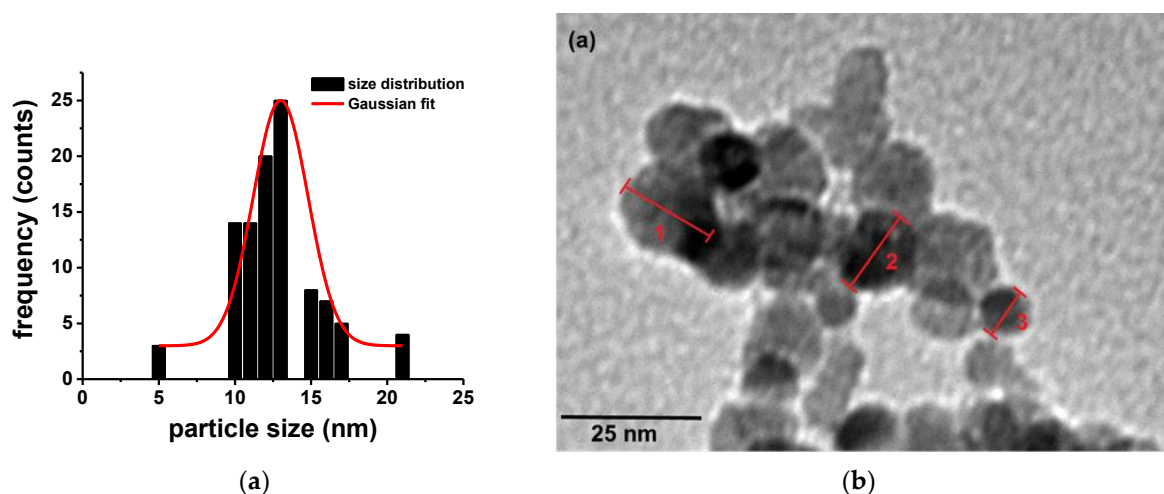
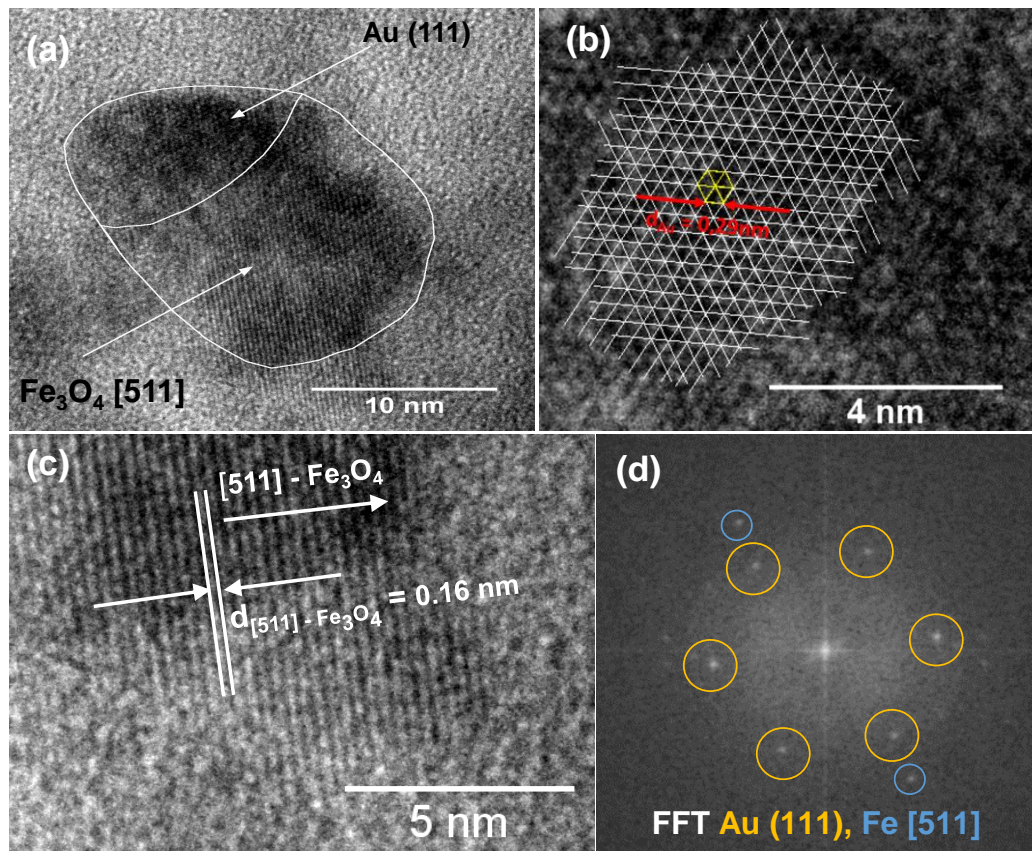


Figure 2. (a) TEM image of the  $\text{Fe}_3\text{O}_4@Au$  pNPs, (b) and their size distribution.

High-resolution transmission electron microscopy (HRTEM) studies, completed by fast Fourier transform (FFT) analyses of the  $\text{Fe}_3\text{O}_4@Au$  pNPs, provided in-depth insight into the spatial distribution of the chemical composition and crystal phases. The HRTEM images of a  $\text{Fe}_3\text{O}_4@Au$  pNP in different magnifications (Figure 3) are depicted as a projection along the (511) direction of the  $\text{Fe}_3\text{O}_4$  nanocrystal (Figure 3a). The  $\text{Fe}_3\text{O}_4$  nanocrystal is partially covered with an Au nanostructure, as it is reflected by the “darker” contrast due to the higher electron density and larger electron-diffracting power of Au in comparison to that of the iron oxide core. The Au composition and structure of the crystalline surface layer were confirmed by the interatomic distance  $d_{Au} = 0.29$  nm, which identifies the crystallographic (111) facet of face-centered cubic gold as having a lattice constant of 0.407 nm (Figure 3b). The distance between two adjacent planes in the  $\text{Fe}_3\text{O}_4$  structure is 0.16 nm which is related to the (511) facets of inverse spinel structured  $\text{Fe}_3\text{O}_4$  (Figure 3c). These results are consistent with the FFT image analysis of

the image phase-contrast variation across the  $\text{Fe}_3\text{O}_4$ -Au pNP, which reveals 6 diffraction spots for the (111) planes of the Au nanopatch and 2 spots for the (511) planes of the  $\text{Fe}_3\text{O}_4$  NP (Figure 3d).



**Figure 3.** (a) HRTEM image of a  $\text{Fe}_3\text{O}_4$ @Au pNP (b,c) with magnified sections, and (d) the fast Fourier transform (FFT) image.

The magnetic properties of the  $\text{Fe}_3\text{O}_4$ @Au pNPs were examined by measuring magnetization curves as a function of the applied magnetic field  $H$  and in dependence on the temperature  $T$ . The magnetization curve in Figure 4a measured at 300 K reflects the superparamagnetic character of the  $\text{Fe}_3\text{O}_4$ @Au pNPs. The magnetization saturation ( $M_S$ ) value of the  $\text{Fe}_3\text{O}_4$ @Au pNPs is 43.6 emu/g. This value is significantly smaller than that (i.e., 66.1 emu/g) derived from the magnetization curves of nearly equally sized  $\text{Fe}_3\text{O}_4$  NPs [30]. The smaller  $M_S$  value can be explained by the magnetically inactive gold surface layer. In addition, the interface communication between the Au nanopatches and the  $\text{Fe}_3\text{O}_4$  core may also partially destroy the magnetization properties of the  $\text{Fe}_3\text{O}_4$  NPs. The superparamagnetic behavior of the  $\text{Fe}_3\text{O}_4$ @Au pNPs is confirmed by the temperature dependence of the zero-field cooled-field cooled (ZFC-FC) magnetization under an applied magnetic field of 0.01 T (Figure 4b). The ZFC curve exhibits a broad maximum indicating the superparamagnetic blocking temperature at 80 K. The broadness of the ZFC curve indicates the existence of a dipolar coupling between nanoparticles due to their proximal distance.

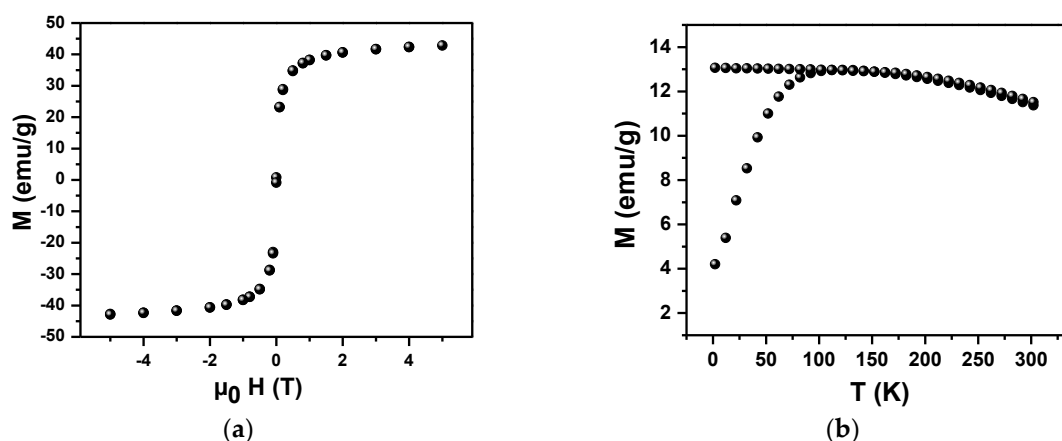


**Figure 4.** (a) Magnetization curve at 300 K and, (b) the temperature dependence of the ZFC/FC magnetization of the  $\text{Fe}_3\text{O}_4@Au$  pNPs.

The UV-Vis absorption spectrum of an aqueous solution of MPA-stabilized  $\text{Fe}_3\text{O}_4@Au$  pNPs (Figure 5) exhibits a broad shoulder between 320 and 420 nm, and a smaller one between 480 and 500 nm. The spectral feature around 490 nm is assigned to the partially masked plasmon resonance band of larger gold nanopatches, whereas the broad shoulder presumably arises from charge transfer across the Au- $\text{Fe}_3\text{O}_4$  interface.

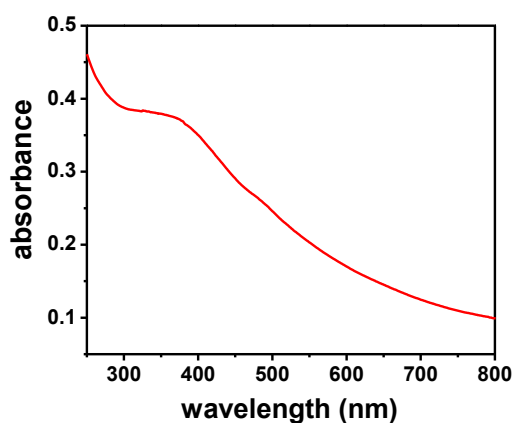


**Figure 5.** UV-Vis absorption spectrum of an aqueous solution of MPA-stabilized  $\text{Fe}_3\text{O}_4@Au$  pNPs.

To improve the water solubility, the MPA-terminated  $\text{Fe}_3\text{O}_4@Au$  pNPs were subsequently coated with 1-methyl-3-(dodecylphosphonic acid) imidazolium (Imidazolium-PA). This amphiphilic surfactant was recently shown to form a self-assembled monolayer on a nanoparticle surface [31]. The FTIR transmission spectra of the MPA-terminated  $\text{Fe}_3\text{O}_4@Au$  pNPs (black line) and the Imidazolium-PA-terminated  $\text{Fe}_3\text{O}_4@Au$  pNPs (red line) are depicted in Figure 6. For MPA-terminated  $\text{Fe}_3\text{O}_4@Au$  pNPs, the two peaks at  $1645$  and  $1532\text{ cm}^{-1}$ , which are ascribed to the symmetric and asymmetric carboxylate ( $\text{COO}^-$ ) stretch, respectively, substantiate that MPA was covalently bound to the  $\text{Fe}_3\text{O}_4$  nanoparticle surface [32]. The absence of the characteristic peak at  $2575\text{ cm}^{-1}$  for the S-H stretching represents an indirect evidence for the formation of the covalent Au-S bond at the gold surface. MPA was very likely bound to both, the  $\text{Fe}_3\text{O}_4$  and Au surface. In case of the surfactant Imidazolium-PA, the predominant peaks at  $991$  and  $1395\text{ cm}^{-1}$  are assigned to the symmetric P-O and P=O stretching vibration, respectively. Furthermore, the  $\text{CH}_2/\text{CH}_3$ -stretching vibrational bands peaking at  $2849$  and  $2920\text{ cm}^{-1}$  indicate the surface binding of Imidazolium-PA for  $\text{Fe}_3\text{O}_4@Au$  pNPs.

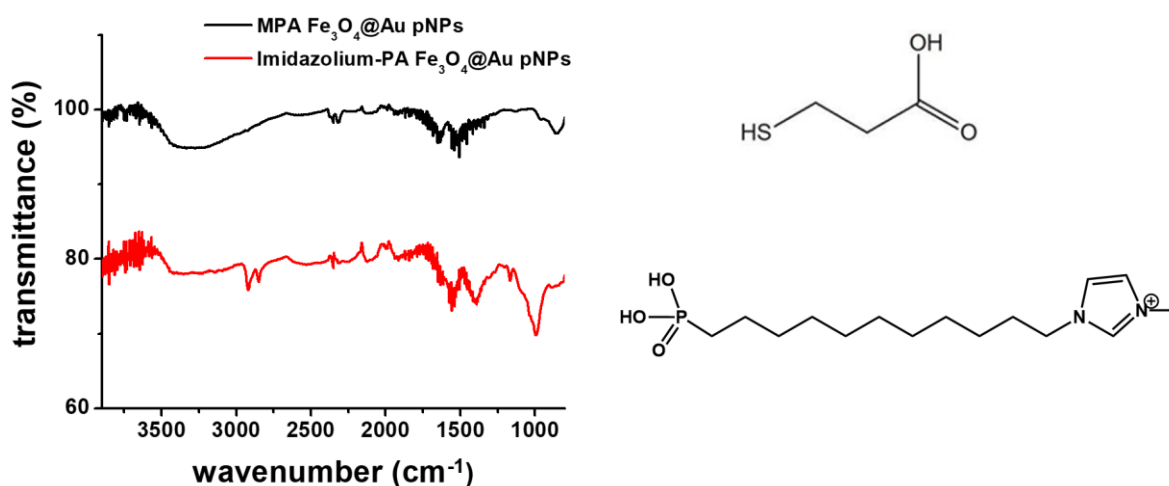


**Figure 6.** FTIR transmission spectra of the Fe<sub>3</sub>O<sub>4</sub>@Au pNPs and the structure formula of the surfactants MPA (top right) and Imidazolium-PA (bottom right).

The cellular uptake of Imidazolium-PA-terminated Fe<sub>3</sub>O<sub>4</sub>@Au pNPs by human breast adenocarcinoma cells (MCF-7 cells) was examined using TEM (Figure 7). Apparently, the TEM image of the MCF-7 cell reveals that Fe<sub>3</sub>O<sub>4</sub>@Au pNPs formed large agglomerates (black spots) within the cytoplasm. These agglomerates were entrapped in cellular vesicles (endosomes) which indicates cellular uptake via endocytosis. The biocompatibility of the Imidazolium-PA-terminated Fe<sub>3</sub>O<sub>4</sub>@Au pNPs was compared with those of Imidazolium-PA-terminated Fe<sub>3</sub>O<sub>4</sub> NPs and MPA-stabilized gold nanoclusters (AuNCs) upon examining their influence on the viability of tumor cells (MCF-7 and adenocarcinomic human alveolar basal epithelial (A459) cells) and healthy cells (human breast epithelial cell line (MCF-10A)) (Figure 8).

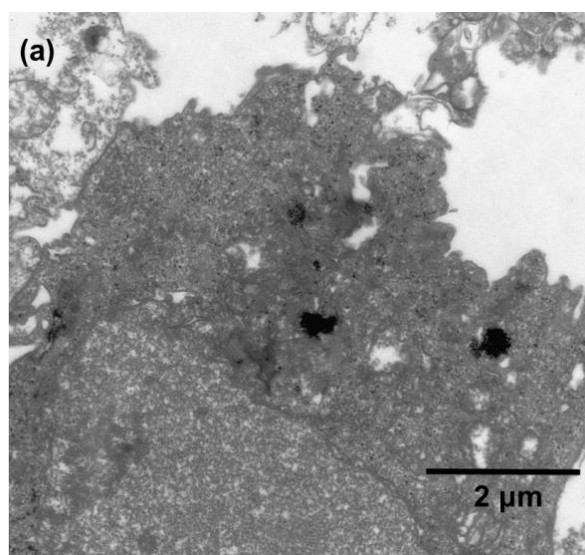


**Figure 7.** TEM image of an MCF-7 cell loaded with Fe<sub>3</sub>O<sub>4</sub>@Au pNPs.

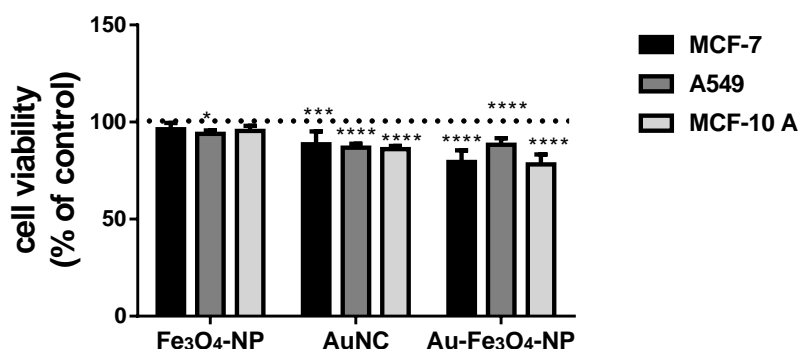


**Figure 8.** Cell viability of MCF-7, A549 and MCF-10A cells loaded with Fe<sub>3</sub>O<sub>4</sub> NPs, AuNC or Fe<sub>3</sub>O<sub>4</sub>@Au pNPs, AuNC ( $n = 6$ , \*  $p < 0.05$ , \*\*\*  $p < 0.001$ , \*\*\*\*  $p < 0.0001$ ).

The respective cell viability data in Figure 8 were obtained by conducting the neutral red assay. The dashed line at 100% represents the viability of the respective control cells. Fe<sub>3</sub>O<sub>4</sub>@Au pNPs at a concentration of 10 µg/mL were found to decrease the viability of MCF-7 and MCF-10A cells down to 80%, whereas the A549 cells were hardly impaired. Intracellular AuNCs were found to diminish the viability of all cell lines under study by 10 to 13%. In contrast, the biocompatibility of the Imidazolium-PA-stabilized Fe<sub>3</sub>O<sub>4</sub> NPs is remarkably high, exhibiting cell viability values of around 95% for the MCF-7, MCF-10A and A549 cells. This is explained by the shielding effect of Imidazolium-PA, which is self-assembled in a monolayer on the Fe<sub>3</sub>O<sub>4</sub> NP surface, obviously preventing the formation of HO• at the Fe<sup>2+</sup> cation-containing surface. The slightly toxic effect of the MPA-ligands apparently provided a lower cell viability value for the AuNC and Fe<sub>3</sub>O<sub>4</sub>@Au pNPs.

To examine the impact of the Fe<sub>3</sub>O<sub>4</sub>@Au pNPs on X-ray-induced formation of the intracellular formation of reactive oxygen species (ROS), MCF-7, A549 and MCF-10A cells were incubated with Fe<sub>3</sub>O<sub>4</sub> NPs, AuNC or Fe<sub>3</sub>O<sub>4</sub>@Au pNPs and subsequently exposed to X-radiation at a single dose of 1 Gy (Figures 9 and 10). The change of the intracellular formation of ROS, in total, as well as that of superoxide anion radical (O<sub>2</sub><sup>•-</sup>) or hydroxyl radical (HO•), in particular, were quantified using the dichlorofluorescein (DCF) assay, mitochondrial superoxide indicator MitoSox™Red, and the 3'-(p-hydroxyphenyl)-fluorescein (HPF) assay, respectively. Whereas MCF-7 cells loaded with Fe<sub>3</sub>O<sub>4</sub> NPs or AuNC did not exhibit any change of ROS and HO• formation, intracellular Fe<sub>3</sub>O<sub>4</sub>@Au pNPs apparently raised the ROS and HO• levels by 40 and 10%, respectively (Figures 9a and 10a). All kinds of nanoparticles were observed to boost the relative O<sub>2</sub><sup>•-</sup> concentration by 30 to 40% (Figure 9b). These results are consistent with the cell viability study (Figure 8) and confirm the highest biocompatibility for the Imidazolium-PA-terminated Fe<sub>3</sub>O<sub>4</sub> NPs. X-ray exposure of the MCF-7 cells at a single dose of 1 Gy resulted into a significant enhancement of the ROS formation for all kinds of nanoparticles. While intracellular Fe<sub>3</sub>O<sub>4</sub>@Au pNPs provided an increase of the ROS concentration by 120%, the Fe<sub>3</sub>O<sub>4</sub>-NPs and AuNC caused an increase of 85% and 60%, respectively (Figure 9a). On the other hand, X-ray irradiation of MCF-7 cells loaded with Fe<sub>3</sub>O<sub>4</sub> NPs provoked O<sub>2</sub><sup>•-</sup> degradation by 20%, which probably occurs through the X-ray-activated Fe<sub>3</sub>O<sub>4</sub> surfaces as requiring H<sub>2</sub>O<sub>2</sub> and O<sub>2</sub><sup>•-</sup> consumption during the Fenton and Haber-Weiss reaction (Figure 10b). In comparison, the intracellular AuNC and Fe<sub>3</sub>O<sub>4</sub>@Au pNPs mediated an increase of the O<sub>2</sub><sup>•-</sup> level by 70% and 20%, respectively. This is due to X-ray-induced emission of photoelectrons and Auger electrons from the AuNC and Au nanopatches, which generated O<sub>2</sub><sup>•-</sup> due to the reduction of nearby oxygen. The HO• formation in MCF-7 cells under X-ray exposure was enhanced by intracellular AuNC by 25%, only, whereas X-ray interactions with intracellular Fe<sub>3</sub>O<sub>4</sub> NP and Fe<sub>3</sub>O<sub>4</sub>@Au pNPs raised the HO• concentration for ca. 80% (Figure 9c). The latter is explained by X-ray-induced activation of the Fe<sub>3</sub>O<sub>4</sub> surfaces, which catalyze the HO• production through the Fenton mechanism (Figure 11a). The X-ray-provoked impact on the ROS formation in different kinds of cells—MCF-7, A549 and MCF-10A cells—when loaded with Fe<sub>3</sub>O<sub>4</sub>@Au pNPs is illustrated in Figure 10b. Apparently, the ROS formation in A549 cells achieved

the highest concentration increase, at 140%, whereas Fe<sub>3</sub>O<sub>4</sub>@Au pNPs in MCF-10A cells enhanced the ROS formation by only 30%. These results are consistent with the observed increases of the HO<sup>•</sup> level in A549 and MCF-10A cells by 100% and 30%, respectively. On the other hand, the O<sub>2</sub><sup>•-</sup> production in A549 and MCF-10A cells containing Fe<sub>3</sub>O<sub>4</sub>@Au pNPs appeared to be hardly altered.

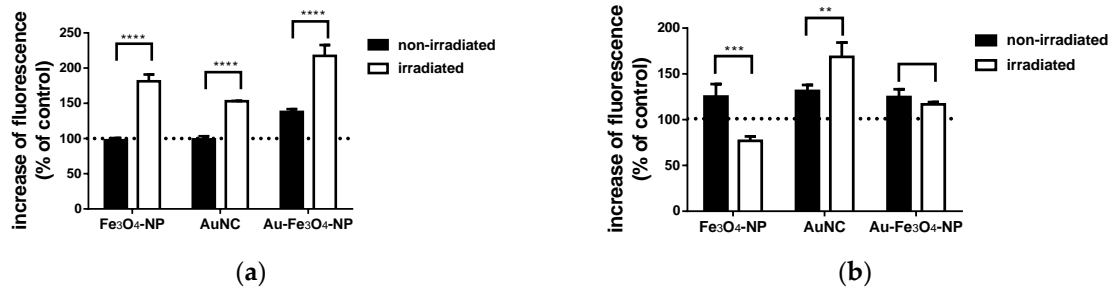


**Figure 9.** (a) Relative ROS, and (b) O<sub>2</sub><sup>•-</sup> concentration in MCF-7 cells loaded with Fe<sub>3</sub>O<sub>4</sub> NPs, AuNC or Fe<sub>3</sub>O<sub>4</sub>@Au pNPs which were exposed to X-radiation at a single dose of 1 Gy or left non-irradiated (*n* = 6, \* *p* < 0.05, \*\*\* *p* < 0.001, \*\*\*\* *p* < 0.0001).

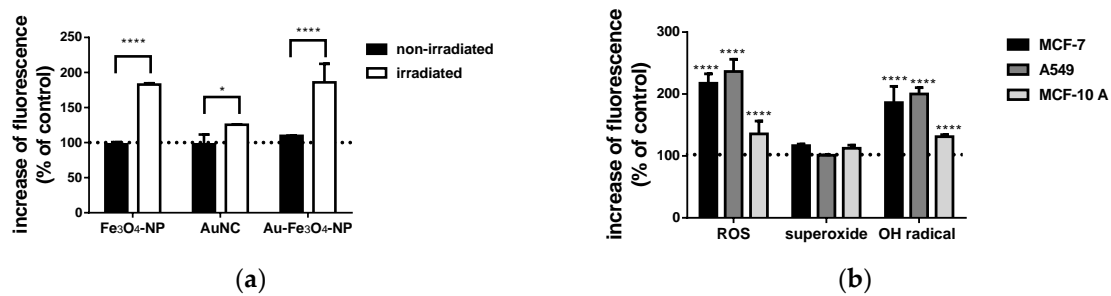


**Figure 10.** (a) Relative HO<sup>•</sup> concentration in MCF-7 cells loaded with Fe<sub>3</sub>O<sub>4</sub> NPs, AuNC or Fe<sub>3</sub>O<sub>4</sub>@Au pNPs which were exposed to X-radiation at 1 Gy or left non-irradiated; (b) relative ROS, O<sub>2</sub><sup>•-</sup> and HO<sup>•</sup> concentration in MCF-7, A549 and MCF-10A cells loaded with Fe<sub>3</sub>O<sub>4</sub>@Au pNPs, which were exposed to X-radiation at 1 Gy (*n* = 6, \* *p* < 0.05, \*\*\* *p* < 0.001, \*\*\*\* *p* < 0.0001).

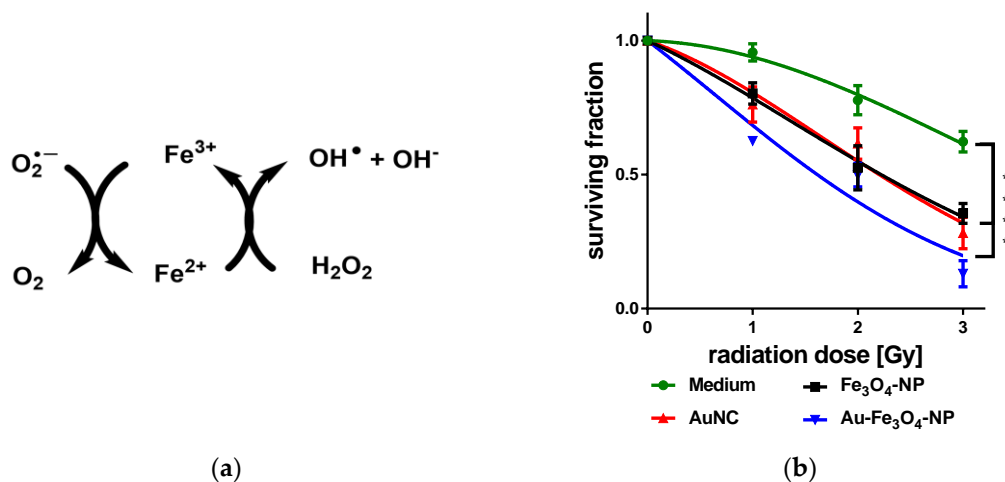


**Figure 11.** Cont.

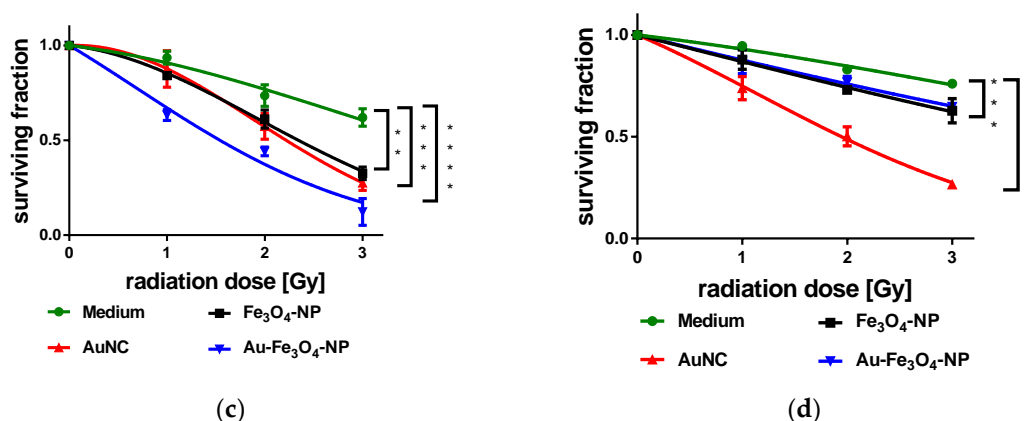


**Figure 11.** (a) Reaction scheme of the  $\text{Fe}^{2+}/\text{Fe}^{3+}$ -catalyzed Fenton reaction and Haber-Weiss cycle; radiation dose survival curves of MCF-7 cells (b), A549 cell (c) and MCF-10A cells (d) in medium (green) and incubated with  $\text{Fe}_3\text{O}_4@Au$  pNPs (blue),  $\text{Fe}_3\text{O}_4$  NPs (black) and AuNC (red).

The clonogenic cell survival assay was employed to survey the impact of the  $\text{Fe}_3\text{O}_4$  NPs, AuNC or  $\text{Fe}_3\text{O}_4@Au$  pNPs on the survival and proliferation of the MCF-7, A549 and MCF-10A cells exposed to X-radiation at single doses of 1, 2, and 3 Gy (Figure 11b,c,d). As expected, the survival curves of irradiated MCF-7 and A549 cells loaded with the diverse kinds of NPs exhibited significantly faster decays than those of the control cells (medium). Amazingly, the AuNC and  $\text{Fe}_3\text{O}_4$  NPs coincided in their influence on the survival behavior of both tumor cell lines, although they enhanced the X-ray-induced generation of two different kinds of ROS. The survival curves obtained for the  $\text{Fe}_3\text{O}_4@Au$  pNP loaded MCF-7 and A549 cells (blue) showed the steepest decays, which are consistent with the associated dose-modifying factor (DMF) values of 0.448 and 0.422 (Table 1). These DMF values are considerably lower than those obtained for the AuNC and  $\text{Fe}_3\text{O}_4$  NP-loaded MCF-7 and A549 cells, which were 0.611 and 0.616, respectively. In contrast, the survival curves of the healthy cells (MCF-10A), when incorporating either  $\text{Fe}_3\text{O}_4@Au$  pNPs or  $\text{Fe}_3\text{O}_4$  NPs, display similar weak decreases and relatively large DMF values of 0.804 and 0.731, whereas intracellular AuNC caused a more quickly decaying survival curve and a rather small DMF value of 0.344.

**Table 1.** DMF values obtained from the radiation dose survival curves of MCF-7, A549 and MCF-10A cells depicted in Figure 10.

DMF	MCF-7	A549	MCF-10A
$\text{Fe}_3\text{O}_4$ -NP	0.616	0.642	0.731
AuNC	0.611	0.607	0.344
$\text{Au-Fe}_3\text{O}_4$ -NP	0.447	0.422	0.804

#### 4. Discussion

Water-soluble, biocompatible patchy  $\text{Fe}_3\text{O}_4$ -Au nanoparticles ( $\text{Fe}_3\text{O}_4@Au$  pNPs) were prepared through a facile one-pot synthesis procedure followed by functionalization with Imidazolium-PA forming a positively charged, self-assembled monolayer on the surface [31]. The one-pot synthesis route started with a redox reaction in acidic solution and was followed by co-precipitation under alkaline conditions. The initial redox reaction between  $\text{Au}^{3+}$  and  $\text{Fe}^{2+}$  cations did not only produce elemental  $\text{Au}^0$  and thereupon, Au nuclei but also  $\text{Fe}^{3+}$  cations which fed the subsequent alkaline co-precipitation process. In the supersaturated acidic reaction solution, AuNCs were formed. The subsequent alkaline co-precipitation provided the formation of  $\text{Fe}_3\text{O}_4$  NPs in the presence of AuNC which epitaxially grew on the surface of the  $\text{Fe}_3\text{O}_4$  NPs, probably under prosecution of the redox reaction. The morphology, composition and surface chemistry, crystallographic, magnetic and optical

properties of the Fe<sub>3</sub>O<sub>4</sub>@Au pNPs were characterized using HRTEM, EDX, and FTIR transmission spectroscopy, XRD, SQUID, and UV-Vis absorption spectroscopy, respectively.

As is evident from the XRD data, HRTEM and EDX analysis, the 12.5 nm-sized Fe<sub>3</sub>O<sub>4</sub>@Au pNPs consist of a spherical monocrystalline Fe<sub>3</sub>O<sub>4</sub> core that is partially coated with crystalline AuNCs and Au nanopatches (Figure 3). Consistently, the Fe<sub>3</sub>O<sub>4</sub>@Au pNPs were found to exhibit superparamagnetism, with a *M<sub>s</sub>* value of 43.6 emu/g, which is smaller than that of nearly equally sized Fe<sub>3</sub>O<sub>4</sub> NPs [30]. This difference is thought to arise from the interface communication between the Au nanopatches and the Fe<sub>3</sub>O<sub>4</sub> core, which partially degrades the magnetization. This is corroborated by the quenching of the surface plasmon resonance band in the UV-Vis absorption spectrum (Figure 5), as indicating interfacial electron transfer from the Au<sup>0</sup> to Fe<sup>3+</sup> cations. As is obvious from the TEM image (Figure 7) displaying agglomerates in endosomes, internalization by MCF-7 cells followed the endocytic pathway. The impact of the different kinds of nanoparticles on the viability of the cancerous MCF-7 and A549 cells and healthy epithelial MCF-10A cells was evaluated by performing the neutral red assay (Figure 8). Imidazolium-PA-stabilized Fe<sub>3</sub>O<sub>4</sub>@Au pNPs at a concentration of 10 µg/mL degraded the viability of MCF-7 and MCF-10A cells by 20%, whereas the A549 cells were hardly damaged. Intracellular AuNC were observed to decrease the viability of MCF-7, A549 and MCF-10A cells to values between 87% and 90%. In contrast, the biocompatibility of the Imidazolium-PA-stabilized Fe<sub>3</sub>O<sub>4</sub> NPs is remarkably high, exhibiting cell viability values of around 95% for all kinds of cells under study. This is due to the shielding effect of Imidazolium-PA, which is self-assembled in a monolayer on the Fe<sub>3</sub>O<sub>4</sub> NP surface, obviously preventing the formation of HO• at the Fe<sup>2+</sup> cation-containing surface. The slightly higher cytotoxicity effect of the Fe<sub>3</sub>O<sub>4</sub>@Au pNPs is explained with the restrained adsorption of the Imidazolium-PA surfactants at the initially MPA-terminated gold nanopatches. The MPA ligands apparently provided lower cell viability values for both the AuNCs and the Fe<sub>3</sub>O<sub>4</sub>@Au pNPs. The performance of the Fe<sub>3</sub>O<sub>4</sub>@Au pNPs as X-ray dosage enhancers was compared with that of the AuNCs and Fe<sub>3</sub>O<sub>4</sub> NPs (Figures 9–11). Therefore, MCF-7, A549 and MCF-10A cells were incubated with the different kinds of nanoparticles and were exposed to X-radiation with single dosages of 1 Gy, 2 Gy, or 3 Gy. The change of the intracellular formation of ROS, in total, and the alteration of the individual O<sub>2</sub>•<sup>-</sup> and HO• productions were determined upon performing the DCF assay, MitoSox<sup>TM</sup>Red, and HPF assay, respectively. X-ray irradiation of the MCF-7 cells at 1 Gy significantly enhanced the ROS formation for all kinds of nanoparticles. Intracellular Fe<sub>3</sub>O<sub>4</sub>@Au pNPs increased the ROS concentration by 120%. On the other hand, the Fe<sub>3</sub>O<sub>4</sub>-NPs and AuNCs only caused increases of 85% and 60%, respectively. Intracellular Fe<sub>3</sub>O<sub>4</sub> NPs and AuNC were observed to preferentially enhance either the HO• or the O<sub>2</sub>•<sup>-</sup> formation in MCF-7 cells only. In comparison, Fe<sub>3</sub>O<sub>4</sub>@Au pNPs elevated the concentration of both O<sub>2</sub>•<sup>-</sup> and HO• in MCF-7 and A549 cells, which indicates the synergistic interplay between the Fe<sub>3</sub>O<sub>4</sub> and Au surfaces for X-ray-induced ROS formation. Moreover, efficient electron transfer across the Au-Fe<sub>3</sub>O<sub>4</sub> interface potentiates the catalytic activity of the Fe<sub>3</sub>O<sub>4</sub> surface by reducing surface Fe<sup>3+</sup> to Fe<sup>2+</sup> cations [27]. The influence of the Fe<sub>3</sub>O<sub>4</sub>@Au pNPs on X-ray-induced ROS formation in the tumor MCF-7 and A549 cells was compared with that in healthy MCF-10A cells. Apparently, the ROS formation in A549 cells containing the Fe<sub>3</sub>O<sub>4</sub>@Au pNPs reached the highest concentration increase being 140%, whereas Fe<sub>3</sub>O<sub>4</sub>@Au pNPs in X-ray irradiated MCF-10A cells enhanced ROS formation by 30% only. These results are consistent with the observed increases of the HO• level in A549 and MCF-10A cells of 100% and 30%, respectively. On the other hand, the X-radiation-induced O<sub>2</sub>•<sup>-</sup> production in A549 and MCF-10A cells loaded with Fe<sub>3</sub>O<sub>4</sub>@Au pNPs appeared to be hardly altered. All these results indicate that the effect of Fe<sub>3</sub>O<sub>4</sub>@Au pNPs on the X-ray enhancement of the ROS production in tumor cells is considerably larger than that in healthy MCF-10A cells.

The clonogenic cell survival assay was employed to survey the impact of the Fe<sub>3</sub>O<sub>4</sub> NPs, AuNC and Fe<sub>3</sub>O<sub>4</sub>@Au pNPs on the survival and proliferation of the MCF-7, A549 and MCF-10A cells exposed to X-radiation at single doses of 1, 2, and 3 Gy. In comparison with the AuNC- and Fe<sub>3</sub>O<sub>4</sub> NP-loaded tumor (MCF-7 and A549) cells, the radiation dose survival curves obtained for the cell lines containing Fe<sub>3</sub>O<sub>4</sub>@Au pNPs showed the steepest decays and the smallest DMF values, at 0.448 and 0.422, respectively. This clearly indicates higher Fe<sub>3</sub>O<sub>4</sub> surface reactivity, which is enhanced by interfacial electron transfer from the surface-grown Au nanopatches. The significantly elevated O<sub>2</sub><sup>•-</sup> level in X-ray-irradiated MCF-7 cells containing Fe<sub>3</sub>O<sub>4</sub>@Au pNPs indirectly substantiates the higher concentration of Fe<sup>2+</sup> cations in the Fe<sub>3</sub>O<sub>4</sub> surface due to the reduction of Fe<sup>3+</sup> cations through interfacial Au<sup>0</sup> atoms. In contrast, the survival curves of the healthy cells (MCF-10A), when incorporating either Fe<sub>3</sub>O<sub>4</sub>@Au pNPs or Fe<sub>3</sub>O<sub>4</sub> NPs, display a similar weak descent and relatively large DMF value, at 0.804 and 0.731, whereas intracellular AuNC caused a fast decay of the survival curve and a rather small DMF value of 0.344. Hence, the survival curves and associated DMF values of the MCF-7 and A549 cells embodying different kinds of nanoparticles confirm the paramount performance of the Fe<sub>3</sub>O<sub>4</sub>@Au pNPs as highly efficient X-ray enhancing agents.

**Author Contributions:** C.K. and S.K. are responsible for the total conceptualization, methodology and supervision of the experiments, C.K. wrote, reviewed and edited the original draft; S.K. performed and described all cell biological experiments and evaluated the experimental data; J.H. developed and verified the novel synthesis route for the preparation Fe<sub>3</sub>O<sub>4</sub>@Au pNPs and is responsible for the EDX, HRTEM, XRD, and spectroscopy experiments, C.M. prepared all kinds of nanoparticles and examined the surface structures, L.V.R.D. facilitates all X-Ray irradiation experiments, and W.N. provided the TEM experiments on MCF-7 cells.

**Funding:** This research received no external funding.

**Acknowledgments:** We thank Andrea Hilpert (Department of Anatomy, Chair of Anatomy I, University of Erlangen) for the TEM studies.

**Conflicts of Interest:** The authors declare no conflict of interest.

## References

1. Shafiq, J.; Barton, M.; Noble, D.; Lemer, C.; Donaldson, L.J. An International review of patient safety measures in radiotherapy practice. *Radiother. Oncol.* **2009**, *92*, 15–21. [[CrossRef](#)] [[PubMed](#)]
2. Yu, J.B.; Cramer, L.D.; Herrin, J.; Soulos, P.R.; Potosky, A.L.; Gross, C.P. Stereotactic body radiation therapy versus intensity-modulated radiation therapy for Prostate Cancer: Comparison of Toxicity. *Clin. Oncol.* **2014**, *32*, 1195–1201. [[CrossRef](#)]
3. Babael, M.; Ganjalikhani, M. The Potential Effectiveness of Nanoparticles as Radio Sensitizers for Radiotherapy. *Bioimpacts* **2014**, *4*, 15–20.
4. Butterworth, K.T.; McMahon, S.J.; Currella, F.J.; Prise, K.M. Physical Basis and Biological Mechanisms of Gold Nanoparticle Radiosensitization. *Nanoscale* **2012**, *4*, 4830–4838. [[CrossRef](#)] [[PubMed](#)]
5. Cooper, D.R.; Bekahand, D.; Nadeau, J.L. Gold Nanoparticles and their Alternatives for Radiation Therapy Enhancement. *Front. Chem.* **2014**, *2*, 2–13. [[CrossRef](#)] [[PubMed](#)]
6. Mesbahi, A. A Review on Gold Nanoparticles Radiosensitization Effect in Radiation Therapy of Cancer. *Rep. Pract. Oncol. Radiother.* **2010**, *15*, 176–180. [[CrossRef](#)] [[PubMed](#)]
7. Misawa, M.; Takahashi, J. Generation of Reactive Oxygen Species Induced by Gold Nanoparticles under X-Ray and UV Irradiations. *J. Nanomed. NBM* **2011**, *7*, 604–614. [[CrossRef](#)]
8. Lee, S.-M.; Tsai, D.-H.; Hackley, V.A.; Brechbiel, M.W.; Cook, R.F. Surface-Engineered Nanomaterials as X-Ray Absorbing Adjuvant Agents for Auger-Mediated Chemo-Radiation. *Nanoscale* **2013**, *5*, 5252–5256. [[CrossRef](#)]
9. Jain, S.; Coulter, J.A.; Hounsell, A.R.; Butterworth, K.T.; McMahon, S.J.; Hyland, W.B.; Muir, M.F.; Dickson, G.R.; Prise, K.M.; Currell, F.J.; et al. Cell-Specific Radiosensitization by Gold Nanoparticles at Megavoltage Radiation Energies. *Int. J. Radiat. Oncol. Biol. Phys.* **2011**, *79*, 531–539. [[CrossRef](#)]
10. Hainfeld, J.F.; Slatkin, D.N.; Smilowitz, H.M. The Use of Gold Nanoparticles to Enhance Radiotherapy in Mice. *Phys. Med. Biol.* **2004**, *49*, N309–N315. [[CrossRef](#)]

11. Kumar, R.; Korideck, H.; Ngwa, W.; Berbeco, R.I.; Makrigiorgos, G.M.; Sridhar, S. Third Generation Gold Nanoplatfrom Optimized for Radiation Therapy. *Transl. Cancer Res.* **2013**, *2*. [[CrossRef](#)]
12. Kunz-Schughart, L.A.; Dubrovskaya, A.; Peitzsch, C.; Ewe, A.; Aigner, A.; Schellenburg, S.; Muders, M.H.; Hampel, S.; Cirillo, G.; Iemma, F.; et al. Nanoparticles for Radiooncology: Mission, Vision, Challenges. *Biomaterials* **2017**, *120*, 155–184. [[CrossRef](#)] [[PubMed](#)]
13. Sicard-Roselli, C.; Brun, E.; Gilles, M.; Baldacchino, G.; Kelsey, C.; McQuaid, H.; Polin, C.; Wardlow, N.; Currell, F. A New Mechanism for Hydroxyl Radical Production in Irradiated Nanoparticle Solutions. *Small* **2014**, *10*, 3338–3346. [[CrossRef](#)] [[PubMed](#)]
14. Imlay, J.A.; Linn, S. DNA Damage and Oxygen Radical Toxicity. *Science* **1988**, *240*, 1302–1309. [[CrossRef](#)] [[PubMed](#)]
15. Klein, S.; Sommer, A.; Distel, L.V.R.; Neuhuber, W.; Kryschi, C. Superparamagnetic iron oxide nanoparticles as radiosensitizer via enhanced reactive oxygen species formation. *Biochem. Biophys. Res. Commun.* **2012**, *425*, 393–397. [[CrossRef](#)] [[PubMed](#)]
16. Klein, S.; Sommer, A.; Distel, L.V.R.; Hazemann, J.-L.; Kröner, W.; Neuhuber, W.; Müller, P.; Proux, O.; Kryschi, C. Superparamagnetic Iron Oxide Nanoparticles as Novel X-Ray Enhancer for Low-Dose Radiation Therapy. *J. Phys. Chem. B* **2014**, *118*, 6159–6166. [[CrossRef](#)] [[PubMed](#)]
17. Leung, K.C.-F.; Xuan, S.; Zhu, X.; Wang, D.; Chak, C.-P.; Lee, S.-F.; Ho, W.K.-W.; Chung, B.C.-T. Gold and Iron Oxide Hybrid Nanocomposite Materials. *Chem. Soc. Rev.* **2012**, *41*, 1911–1928. [[CrossRef](#)]
18. Zhou, L.; Yuan, J.; Wei, Y. Core-Shell Structural Iron Oxide Hybrid Nanoparticles: From Controlled Synthesis to Biomedical Applications. *J. Mater. Chem.* **2011**, *21*, 2823–2840. [[CrossRef](#)]
19. Mandal, M.; Kundu, S.; Ghosh, S.K.; Panigrahi, S.; Sau, T.K.; Yusuf, S.M.; Pal, T. Magnetite Nanoparticles with Tunable Gold or Silver Shell. *J. Colloid Interface Sci.* **2005**, *286*, 187–194. [[CrossRef](#)]
20. Cho, S.-J.; Jarrett, B.R.; Louie, A.Y.; Kauzlarich, S.M. Gold-Coated Iron Nanoparticles: A Novel Magnetic Resonance Agent for T<sub>1</sub> and T<sub>2</sub> Weighted Imaging. *Nanotechnology* **2006**, *17*, 640–644. [[CrossRef](#)]
21. Maleki, H.; Simchi, A.; Imani, M.; Costa, B.F.O. Size-Controlled Synthesis of Superparamagnetic Iron Oxide Nanoparticles and their Surface Coating by Gold for Biomedical Applications. *J. Magn. Magn. Mater.* **2012**, *324*, 3997–4005. [[CrossRef](#)]
22. Zhao, X.; Cai, Y.; Wang, T.; Shi, Y.; Jiang, G. Preparation of Alkanethiolate-Functionalized Core/Shell Fe<sub>3</sub>O<sub>4</sub>@Au Nanoparticles and Its Interaction with Several Typical Target Molecules. *Anal. Chem.* **2008**, *80*, 9091–9096. [[CrossRef](#)] [[PubMed](#)]
23. Gao, J.; Gu, H.; Xu, B. Multifunctional Magnetic Nanoparticles: Design, Synthesis, and Biomedical Applications. *Acc. Chem. Res.* **2009**, *42*, 1097–1107. [[CrossRef](#)] [[PubMed](#)]
24. Hoskins, C.; Min, Y.; Gueorguieva, M.; McDougall, C.; Volovick, A.; Prentice, P.; Whang, Z.; Melzer, A.; Cuschieri, A.; Wang, L. Hybrid Gold-Iron Oxide Nanoparticles as a Multifunctional Platform for Biomedical Application. *J. Nanobiotechnol.* **2012**, *10*. [[CrossRef](#)] [[PubMed](#)]
25. Kostevsek, N.; Locatelli, E.; Garrovo, C.; Arena, F.; Monaco, I.; Nikolov, I.P.; Sturm, S.; Rozman, K.Z.; Lorusso, V.; Giustetto, P.; et al. The One-Step Synthesis and Surface Functionalization of Dumbbell-like Gold–Iron Oxide Nanoparticles: A Chitosan-Based Nanotheranostic System. *Chem. Commun.* **2016**, *52*, 378–381. [[CrossRef](#)]
26. Pineider, F.; de Julián Fernández, C.; Videtta, V.; Carlino, E.; Al Hourani, A.; Wilhelm, F.; Rogalew, A.; Cozzoli, P.D.; Ghigna, P.; Sangregorio, C. Spin-Polarization Transfer in Colloidal Magnetic-Plasmonic Au/Iron Oxide Hetero-nanocrystals. *ACS Nano* **2013**, *7*, 857–866. [[CrossRef](#)] [[PubMed](#)]
27. Klein, S.; Harreiss, C.; Menter, C.; Hümmer, J.; Distel, L.V.R.; Meyer, K.; Hock, R.; Kryschi, C. NOBF<sub>4</sub>-Functionalized Au-Fe<sub>3</sub>O<sub>4</sub> Nanoheterodimers for Radiation Therapy: Synergy Effect Due to Simultaneous Reactive Oxygen and Nitrogen Species Formation. *ACS Appl. Mater. Interfaces* **2018**, *10*, 17071–17080. [[CrossRef](#)] [[PubMed](#)]
28. Massart, R. Preparation of Aqueous Magnetic Liquids in Alkaline and Acidic Media. *IEEE Trans. Magn.* **1981**, *17*, 1247–1248. [[CrossRef](#)]
29. Cho, S.-J.; Idrobo, J.-C.; Olamit, J.; Liu, K.; Browning, N.D.; Kauzlarich, S.M. Growth Mechanisms and Oxidation Resistance of Gold-Coated Iron Nanoparticles. *Chem. Mater.* **2005**, *17*, 3181–3186. [[CrossRef](#)]
30. Goya, G.F.; Berquó, T.S.; Fonseca, F.C.; Morales, M.P. Static and Dynamic Magnetic Properties of Spherical Magnetite Nanoparticles. *J. Appl. Phys.* **2003**, *94*, 23520–23528. [[CrossRef](#)]

31. Klein, S.; Kizaloglu, M.; Portilla, L.; Park, H.; Rejek, T.; Hümmer, J.; Meyer, K.; Hock, R.; Distel, L.V.R.; Halik, M.; et al. Enhanced In Vitro Biocompatibility and Water Dispersibility of Magnetite and Cobalt Ferrite Nanoparticles Employed as ROS Formation Enhancer in Radiation Cancer Therapy. *Small* **2018**, *14*, 1704111. [[CrossRef](#)] [[PubMed](#)]
32. Yee, C.; Kataby, A.; Ulman, T.; Prozorov, H.; White, A.; King, A.; Rafailovich, M.; Sokolov, J.; Gedanken, A. Self-Assembled Monolayers of Alkanesulfonic and -phosphonic Acids on Amorphous Iron Oxide Nanoparticles A. *Langmuir* **1999**, *15*, 7111–7115. [[CrossRef](#)]



© 2018 by the authors. Licensee MDPI, Basel, Switzerland. This article is an open access article distributed under the terms and conditions of the Creative Commons Attribution (CC BY) license (<http://creativecommons.org/licenses/by/4.0/>).